## **OPEN ACCESS**



# Acceleration and Expansion of a Coronal Mass Ejection in the High Corona: Role of Magnetic Reconnection

Bin Zhuang <sup>1</sup> , Noé Lugaz <sup>1</sup> , Manuela Temmer <sup>2</sup> , Tingyu Gou <sup>3</sup> , and Nada Al-Haddad <sup>1</sup> 

1 Institute for the Study of Earth, Oceans, and Space, University of New Hampshire, Durham, NH, USA; bin.zhuang@unh.edu, noe.lugaz@unh.edu

2 Institute of Physics, University of Graz, A-8010 Graz, Austria

3 CAS Key Laboratory of Geospace Environment, Department of Geophysics and Planetary Sciences, University of Science and Technology of China, Hefei 230026,

People's Republic of China
Received 2021 November 11; revised 2022 May 31; accepted 2022 June 3; published 2022 July 13

#### **Abstract**

The important role played by magnetic reconnection in the early acceleration of coronal mass ejections (CMEs) has been widely discussed. However, as CMEs may have expansion speeds comparable to their propagation speeds in the corona, it is not clear whether and how reconnection contributes to the true acceleration and expansion separately. To address this question, we analyze the dynamics of a moderately fast CME on 2013 February 27, associated with a continuous acceleration of its front into the high corona, even though its speed had reached ~700 km s<sup>-1</sup>, which is faster than the solar wind. The apparent acceleration of the CME is found to be due to its expansion in the radial direction. The true acceleration of the CME, i.e., the acceleration of its center, is then estimated by taking into account the expected deceleration caused by the drag force of the solar wind acting on a fast CME. It is found that the true acceleration and the radial expansion have similar magnitudes. We find that magnetic reconnection occurs after the eruption of the CME and continues during its propagation in the high corona, which contributes to its dynamic evolution. Comparison between the apparent acceleration related to the expansion and the true acceleration that compensates the drag shows that, for this case, magnetic reconnection contributes almost equally to the expansion and to the acceleration of the CME. The consequences of these measurements for the evolution of CMEs as they transit from the corona to the heliosphere are discussed.

Unified Astronomy Thesaurus concepts: Solar coronal mass ejections (310)

#### 1. Introduction

Coronal mass ejections (CMEs) are large-scale eruptions of coronal plasma and magnetic fluxes ejected into the heliosphere. The speed of CMEs ranges from  $\sim 100$  to  $3500 \, \mathrm{km \, s}^{-1}$ (Lamy et al. 2019), and fast CMEs (e.g., speed >800 km s<sup>-1</sup>) are of great interest for their role in causing extreme space weather events (e.g., Kilpua et al. 2019; Zhuang et al. 2018, 2020). Typically, CMEs are found to undergo three phases of dynamic evolution: (1) an initiation phase with a slow rise, (2) an impulsive phase with a fast acceleration, and (3) a propagation phase with a constant or slowly decreasing speed (Zhang et al. 2001, 2004; Temmer et al. 2008, 2010). During these three phases, the dominant force acting on CMEs is different (e.g., Vršnak et al. 2004b; Michalek et al. 2015), i.e., the Lorentz force competing with the drag force of the solar wind (solar gravity can be neglected), as further explained below.

In the low corona where magnetic pressure is dominant over thermal pressure, the Lorentz force accounts for the initiation and initial acceleration of the CME (e.g., Forbes 2000). The acceleration usually takes place impulsively within a few to tens of minutes with magnitudes varying from  $\sim$ 200 to  $\sim$ 7000 m s<sup>-2</sup> (e.g., Zhang et al. 2001, 2004; Vršnak et al. 2007; Temmer et al. 2008), and leads to fast CMEs associated with solar flares. Two temporal correlations, i.e., (1) between the soft X-ray flux of solar flares and the CME speed profile (e.g., Zhang et al. 2001, 2004; Vršnak et al. 2004a), and (2) between

Original content from this work may be used under the terms of the Creative Commons Attribution 4.0 licence. Any further distribution of this work must maintain attribution to the author(s) and the title of the work, journal citation and DOI.

the hard X-ray flux of flares and the acceleration profile of fast CMEs (Temmer et al. 2008, 2010; Veronig et al. 2018; Gou et al. 2020; Zhu et al. 2020), have revealed a close flare–CME relationship. Flares and CMEs are coupled through the action of magnetic reconnection (e.g., Gou et al. 2020). On the one hand, magnetic reconnection can result in a very large release of energy, which contributes to the plasma heating and the acceleration of solar energetic particles in flares. On the other hand, reconnection plays a significant role in the CME acceleration, which is achieved via reducing the tension force owing to the overlying magnetic loops and providing additional magnetic (especially poloidal) flux to the original CME structure (Lin & Forbes 2000; Lin et al. 2004; Vršnak 2008).

At larger distances where coronal magnetic field decreases significantly and the solar wind has reached a faster speed, CMEs primarily experience an aerodynamic drag force due to interaction with the solar wind. This aerodynamic drag force accelerates slow CMEs but decelerates fast CMEs (e.g., Gopalswamy et al. 2000; Vršnak 2001; Cargill 2004; Vršnak & Žic 2007; Vršnak et al. 2007; Subramanian et al. 2012; Sachdeva et al. 2015). In this paper, the term slow (fast) refers to the condition where a CME travels slower (faster) than the solar wind, which typically has a speed of  $\sim 400-500 \,\mathrm{km \, s^{-1}}$ . Previous studies have shown that most fast CMEs reach their peak speed in the low to middle corona ( $<10 R_{\odot}$ ) (e.g., Zhang et al. 2001, 2004; Vršnak et al. 2007; Temmer et al. 2010; Bein et al. 2011; Song et al. 2013). In this paper, we present an event for which the acceleration of a moderately fast CME clearly remains positive for around five hours in the high corona, and we then study the mechanism acting on the continuous acceleration of the CME.

The CME speed in previous studies is usually derived from height-time measurements in coronagraphic images where the height is determined at the CME front (leading edge). However, since CMEs are known to have substantial expansion (e.g., Farrugia et al. 1993; Patsourakos et al. 2010a; Lugaz et al. 2017; Balmaceda et al. 2020), the speed of the CME front in the direction of propagation is the sum of the bulk speed indicative of the propagation of the CME center and the expansion speed relative to the center. Balmaceda et al. (2020) analyzed a sample of 475 CMEs and found that the median expansion speed can reach  $\sim 200-300 \,\mathrm{km \, s^{-1}}$  in the corona, which is comparable to the magnitude of the bulk speed. Therefore, investigating the role of magnetic reconnection in CME dynamics by measuring the variation of the CME front would inevitably incorporate the effect of CME expansion. That is to say, magnetic reconnection leading to the true acceleration and expansion of the CME would both contribute to the variation in speed at the CME front (leading edge). Furthermore, physical processes describing how magnetic reconnection contributes to CME expansion have not been investigated in depth, especially with quantitative measurements. One interpretation proposed by Lin et al. (2004) is that the reconnected magnetic flux accounts for the rapid expansion of the CME, and the plasma flowing out of the current sheet fills the outer shell of the CME. Readers can also refer to Section 5 for a discussion and a sketch about the broadening of the outer shell of the CME through the addition of plasma and magnetic flux associated with magnetic reconnection. In addition to the expansion in the radial direction, CMEs are found to undergo lateral expansion with magnitude similar to or larger than the radial expansion in the corona (e.g., Schwenn et al. 2005; Michalek et al. 2009; Patsourakos et al. 2010a, 2010b; Cheng et al. 2013; Veronig et al. 2018; Balmaceda et al. 2020).

In this paper, we study a CME event that occurred on 2013 February 27. The CME undergoes a long-duration acceleration in the high corona from  $\sim\!10$  to  $>\!20\,R_\odot$ , even though in this height range its speed is found to be substantially greater than the solar wind speed. Signatures of magnetic reconnection on the solar surface are found after the launch of the CME, which provides us with a chance to study its contribution to the acceleration and expansion of the CME in the high corona. Section 2 introduces the instruments and the CME event. Section 3 studies the CME dynamics. Section 4 analyzes the separate contribution of magnetic reconnection. Sections 5 and 6 provides discussion and conclusions.

# 2. Observation

# 2.1. Data and Instrument

We use Large Spectrometric the Angle and Coronagraph (LASCO, Brueckner et al. 1995) on board the Solar and Heliospheric Observatory (SOHO, Domingo et al. 1995) to study the dynamic evolution of the CME. LASCO C2 and C3 have a field of view (FOV) of  $1.5-6 R_{\odot}$  and  $3.7-30 R_{\odot}$ , respectively. We also use the Sun-Earth Connection Coronal and Heliospheric Investigation (SECCHI, Howard et al. 2008) on board the "Ahead" and "Behind" satellites of the Solar Terrestrial Relations Observatory (STEREO, Kaiser et al. 2008), including COR1 and COR2 coronagraphs, and the Extreme Ultraviolet Imager (EUVI). During the eruption of the CME under study, STEREO-A and STEREO-B were located at

 $131^{\circ}$  and  $-139^{\circ}$  longitudinally in Heliocentric Earth Ecliptic coordinates. In situ solar wind parameters at 1 au are taken from the OMNI/Wind database.

# 2.2. Event Overview

The event under study originates from the west solar limb (as seen from Earth) on 2013 February 27. Figures 1(a) and (b) show the running-difference images of the CME in LASCO C2 and C3 at two different times. The three-part structure, i.e., a bright expanding loop, followed by a relatively dark cavity and a bright core (Illing & Hundhausen 1986; Gibson et al. 2006), is clearly observed. The faint front ahead of the sharp bright front (leading edge) of the CME may refer to the shock structure (e.g., Vourlidas et al. 2003), indicated by the dashed green curve in Figure 1(b). Figures 1(c)-(h) show the observations by STEREO-A/EUVI at 195 Å and 304 Å wavelengths. This CME is related to a filament eruption from a quiet solar region that launches at around 04:00 UT as observed by STEREO-A/EUVI 304 Å. CME signatures in white light appear first in LASCO C2 at 04:48 UT. Posteruption arcades in EUVI 195 Å and two bright ribbons in EUVI 304 Å are observed after the CME rises. Since this CME could be observed by LASCO, STEREO-A, and STEREO-B simultaneously, we use the graduated cylindrical shell (GCS) model (Thernisien et al. 2006, 2009) to obtain its threedimensional propagation parameters. We first focus on the direction of propagation, which is S12W86 according to the GCS model. It indicates that this CME is an ideal limb event for LASCO observations, and thus we are able to directly analyze the CME dynamics in the LASCO FOV with minimal projection effects.

# 3. CME Dynamics

# 3.1. Long-duration CME Acceleration in the High Corona

We carefully measure the heights of the CME front and core along the position angle of 255° in LASCO C2 and C3 FOVs (note that \$12 as derived from GCS roughly corresponds to the projected position angle of 255°). In Figures 1(a) and (b), the yellow line indicates the selected position angle, and the green and black diamonds mark the locations of the front and core, respectively. In the following analysis, we presume that the core is located near the CME axis in the LASCO FOV, and we refer to the discussion for detailed interpretations. The heighttime measurements of the front and core are shown in Figure 2(b). Since the CME becomes increasingly fainter during its outward propagation, here we set the uncertainties in measuring the height as increasing linearly from  $\pm 0.023 R_{\odot}$ (i.e., plus/minus two pixels) for the initial data point in the C2 image to  $\pm 0.25 R_{\odot}$  (i.e., plus/minus four pixels) for the final one in the C3 image.

The data points are then fitted linearly (solid line) and quadratically (dashed line). The errors below are the  $1\sigma$  uncertainty from the fits. The linear fit indicates that the CME front has an average speed significantly larger than that of the core, i.e.,  $602\pm89~\rm km~s^{-1}$  versus  $471\pm20~\rm km~s^{-1}$ . This suggests that the CME expands radially with an average speed of  $131\pm91~\rm km~s^{-1}$ . The quadratic fit shows that the speed of the front at  $20~R_{\odot}$  is  $735\pm26~\rm km~s^{-1}$  and greater than the linearly fitted speed, and that the front has a positive acceleration of  $a=14.0\pm1.0~\rm m~s^{-2}$ . These results are consistent with those measured by the Coordinated Data

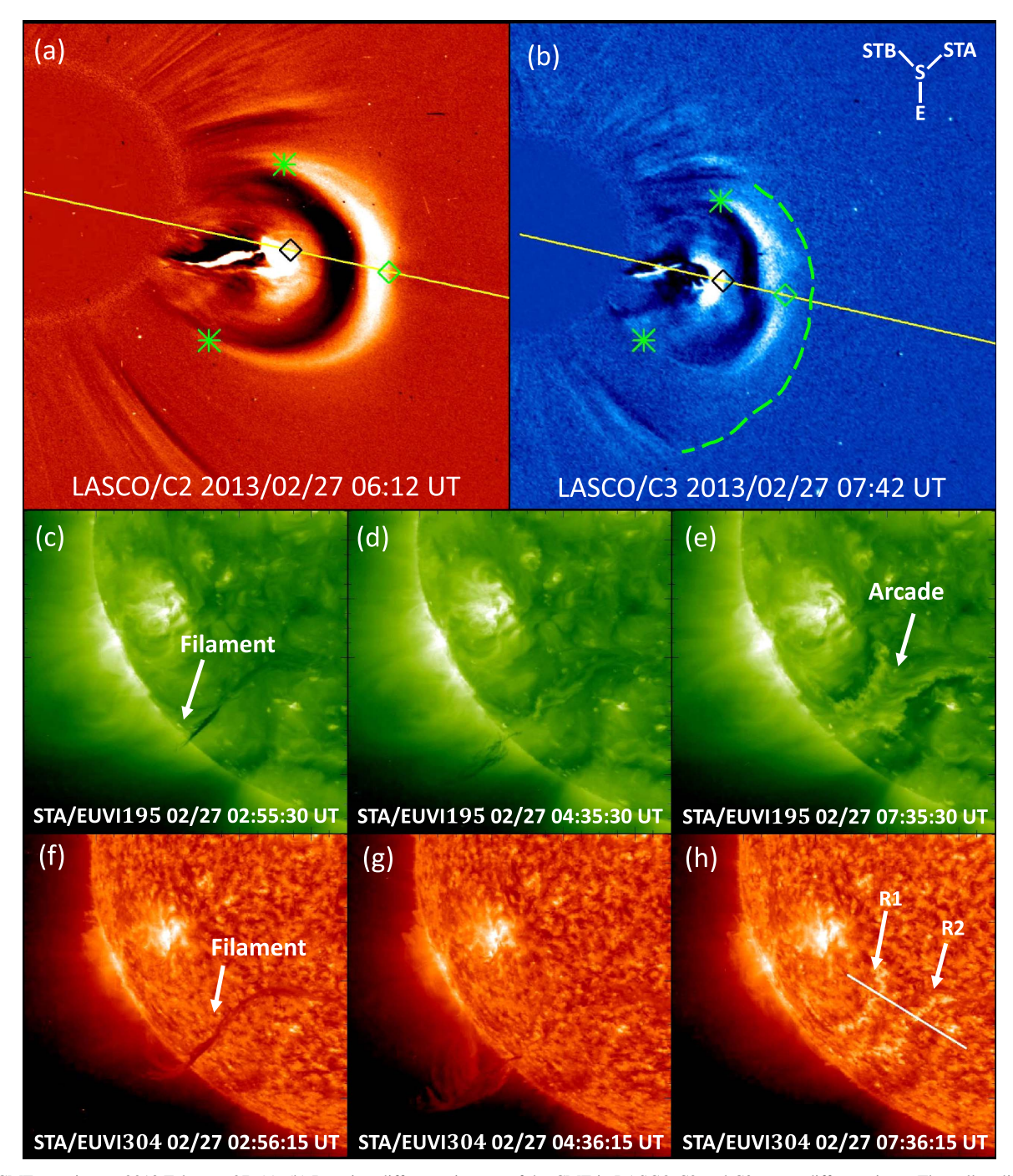


**Figure 1.** CME eruption on 2013 February 27. (a), (b) Running-difference images of the CME in LASCO C2 and C3 at two different times. The yellow line indicates the position angle used for the height measurement, the black and green diamonds indicate the CME core and front, and the two green asterisks mark the two lateral points. In panel (b), the dashed green curve indicates the shock front, and the inset shows the positions of STEREO-A and STEREO-B relative to the Sun (S) and Earth (E). Panels (a) and (b) show heliocentric distance ranges of 1-6  $R_{\odot}$  and 1-17  $R_{\odot}$ , respectively. (c)–(h) Observations of STEREO-A/EUVI at 195 Å and 304 Å. The solid line in panel (h) refers to the position of the superposed slit.

Analysis Workshop CME catalog, but the magnitudes are slightly smaller than those in the catalog because the catalog measures the relatively faint front of the shock structure. As for the core, the quadratic-fit speed is similar to the linear-fit speed, i.e.,  $507 \pm 20 \, \mathrm{km \, s^{-1}}$  versus  $471 \pm 20 \, \mathrm{km \, s^{-1}}$ , associated with a smaller acceleration of  $a = 2.5 \pm 0.6 \, \mathrm{m \, s^{-2}}$ .

We then obtain the speed-time and speed-height variations in Figures 2(c) and (d), respectively. The speed at each time step is derived from a linear fit to three successive height-time measurements, and thus there are no speed data points for the

first and final time steps. The dashed lines in Figure 2(c) show the speed derived from the quadratic fit to the height-time measurements, which indicate a linearly increased front speed and a constant core speed. It is also found that the front and the core experience two propagation phases, i.e., an impulsive acceleration (Phase I) followed by a constant-speed propagation for the core and a smooth acceleration for the front (Phase II). Based on the change in speed of the CME front, the two phases are separated by the time at  $\sim$ 06:50 UT and the height of  $\sim$ 6.5  $R_{\odot}$ , which are indicated by the vertical dashed black

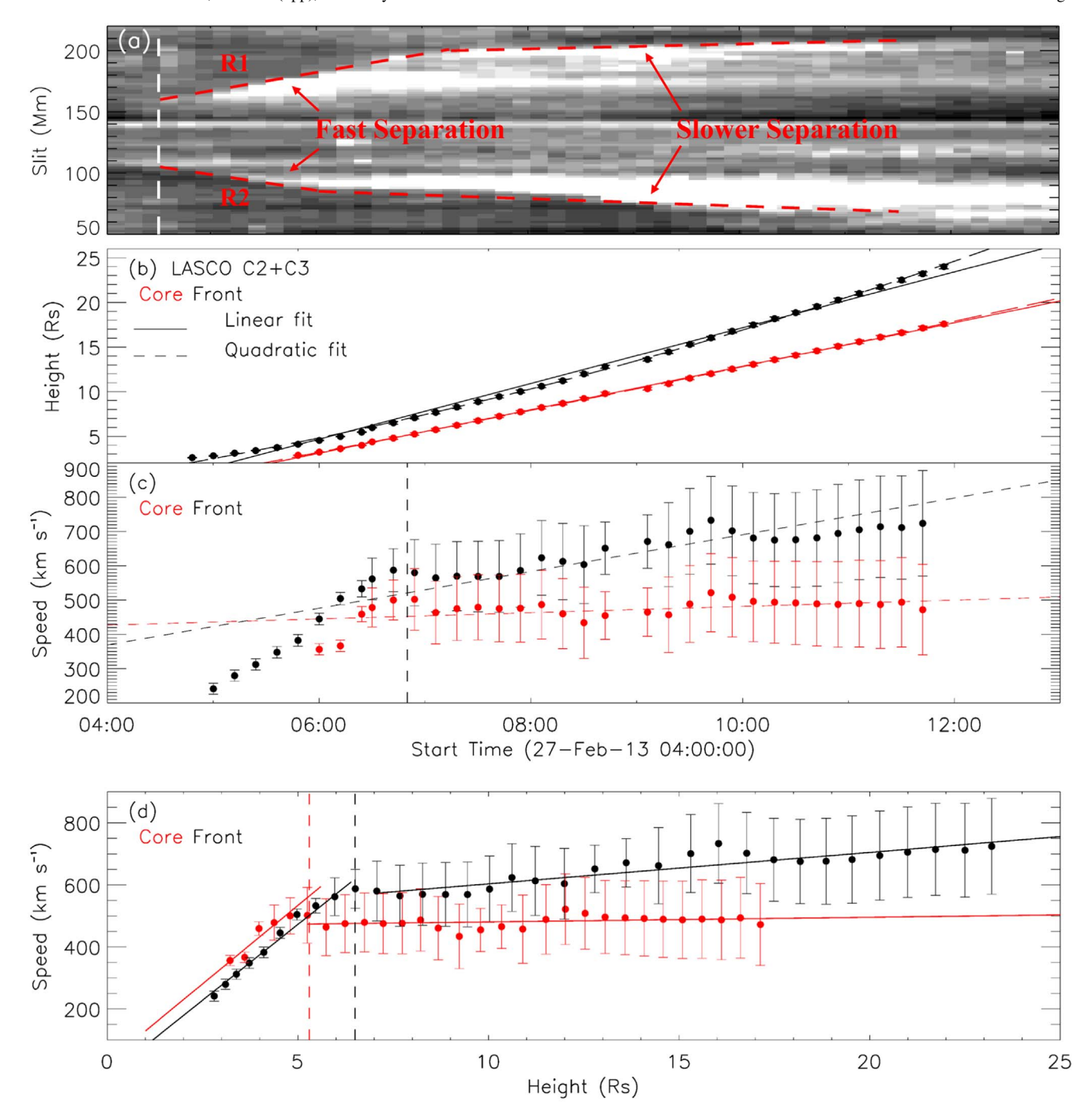
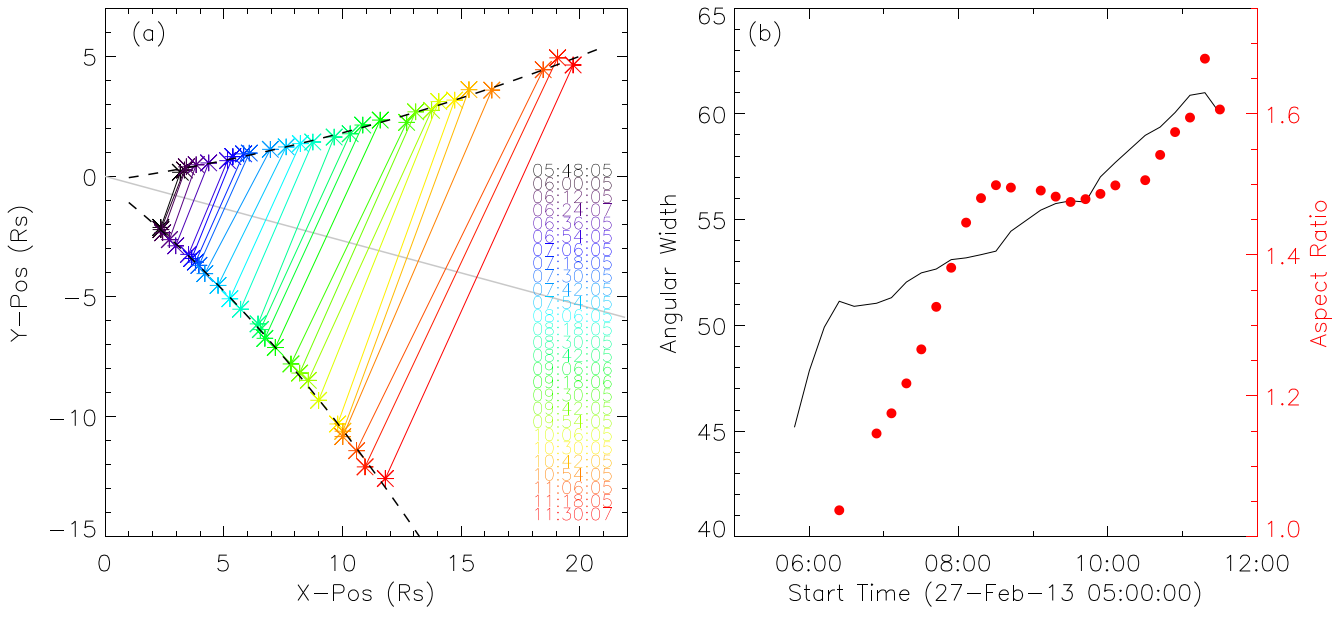


Figure 2. (a) Base-difference image of the slit in STEREO-A/EUVI at 304 Å. Separation of the two ribbons is indicated by the dashed red lines. The vertical dashed line marks the first appearance time of the two ribbons. (b) Height-time measurement of the CME front (black) and core (red), associated with the results from a linear fit (solid line) and a quadratic fit (dashed line). (c) Speed-time measurement. The dashed lines indicate the speed obtained from the quadratic fit in panel (b). (d) Height-speed measurement. The vertical black line indicates the height of the front at  $6.5 R_{\odot}$ , and the red one indicates the height of the core at the same time. The solid lines are the linear-fit results.

line in Figures 2(c) and 2(d). The vertical dashed red line in Figure 2(d) indicates the height of the core at 06:50 UT. The speed–time and speed–height data points in the two phases are then linearly fitted, and shown by the solid lines in Figure 2(d). In Phase I,  $a = 59.1 \pm 3.7$  m s<sup>-2</sup> for the front, and  $a = 65.2 \pm 11.4$  m s<sup>-2</sup> for the core. The acceleration magnitudes are the same for both the core and the front. In Phase II,  $a = 10.1 \pm 4.7$  m s<sup>-2</sup> for the front, which is much higher than  $a = 1.0 \pm 0.7$  m s<sup>-2</sup> for the core, indicating that in this height

range the CME front continues accelerating while the core can be approximated as propagating with a constant speed.

We focus on Phase II, and emphasize here again that this long-duration acceleration is seen although the speed of the front at the start of Phase II is  $\sim 600 \, \mathrm{km \, s^{-1}}$  and larger than the expected solar wind speed at this height of  $6.5 \, R_{\odot}$  (see Section 4 for the estimation of the solar wind speed). The acceleration of the CME front here lasts for nearly five hours as the CME propagates in the high corona. To the best of our



**Figure 3.** (a) Variation of the lateral width of the CME at different times in the X-Y plane. The black solid line indicates the position angle of  $255^{\circ}$ , and the two curves show the quadratic fit to the X-Y data points. (b) Variation of the angular width of the CME (black) and the aspect ratio (red).

knowledge, this is the first reported instance of a CME that continues to accelerate in the high corona, and even to  $>20\,R_\odot$ , though it is already faster than the solar wind. Although the acceleration is not as large as that in Phase I, the long duration of acceleration leads to: (1) the front speed increases by  $\sim 170\,\mathrm{km\,s^{-1}}$  as the CME propagates in the high corona, and (2) the "final" speed reaches  $700\,\mathrm{km\,s^{-1}}$  and above. Furthermore, the comparison between the acceleration of the front and that of the core indicates that the apparent acceleration in observations of the CME front in Phase II is primarily caused by a radial expansion with an acceleration of  $a_{\rm meas} = 9.1 \pm 4.8\,\mathrm{m\,s^{-2}}$ . If not for this expansion, the core would accelerate at the same rate due to the frozen-in conditions in the CME plasma.

Looking at the uncertainties in the CME speed, the finding about the continuous acceleration of the CME in the high corona may be questioned. To confirm that the main result holds, we perform the following calculations. Since the uncertainties come from the height measurement in coronagraphs, we obtain the acceleration by quadratically fitting the height-time measurements for the CME starting from larger distances, e.g., 15 and  $20 R_{\odot}$ . This fitted acceleration is still around  $10 \,\mathrm{m \, s^{-2}}$ . Furthermore, since the CME front becomes fainter as it propagates outward while the true leading edge might not be discernible, the height of the front as located in coronagraphs may be lower than the true one. These two points would further support that the idea that the continuous acceleration of the CME front is true in the high corona. In addition, the CME front is too faint to be distinguished above  $25 R_{\odot}$ , which may bring even larger uncertainties, and thus it is still unclear whether this CME has reached its final speed at this height.

# 3.2. Lateral Expansion of the CME

We turn our attention to the magnitude of the lateral expansion of the CME, which should occur jointly with the radial expansion. The lateral width of the CME is calculated as the length of the line connecting the two asterisks as shown in Figures 1(a) and (b). The two asterisks at each time step mark

the outermost locations of both side-edges of the CME. Figure 3(a) shows the variations of the lateral length associated with the asterisks at different times (varying with colors) in the X-Y plane, where the origin indicates the center of the Sun. The solid black line indicates the position angle of 255°, which is found to be approximately perpendicular to those lateral lines. The two dashed curves correspond to the quadratic fits to the upper and lower sets of asterisks. A linear fit to half of the lateral length shows that the lateral expansion of the CME at one side-edge has an average speed of 260 ( $\pm$ 17) km s<sup>-1</sup>, while a quadratic fit reveals that the acceleration of the expansion at one side is 14.7 ( $\pm$ 2.3) m s<sup>-2</sup>. These indicate that the CME has a stronger lateral expansion than radial expansion, and such a positive acceleration confirms that the lateral expansion occurs jointly with the radial one.

Figure 3(b) shows the variation of the angular width  $(\omega)$ , which is the total width between the two asterisks. It is found that  $\omega$  increases by  $\sim \! 10^\circ$  in Phase II, to reach  $\sim \! 60^\circ$  at  $\sim \! 20\,R_\odot$ . Again, the CME might continue to expand laterally beyond  $20\,R_\odot$ . The aspect ratio, i.e., the ratio of half of the lateral length to the radial length from the core to the front, is shown in Figure 3(b). The aspect ratio increases impulsively at first, and then stays approximately constant at 1.5–1.6. A ratio greater than unity indicates that the cross section of the CME is an ellipse with the major axis in the lateral direction and the minor axis in the radial direction. The aspect ratio  $> \! 1$  is consistent with the above results that the speed and acceleration in the lateral direction are larger than those in the radial direction.

# 3.3. Magnetic Reconnection Associated with the CME Eruption

Signatures of magnetic reconnection on the solar surface are visible after the CME eruption. Two ribbons start brightening at around 05:00 UT in STEREO-A/EUVI 304 Å images, associated with a post-eruption arcade in 195 Å images, as shown in Figures 1(e) and (h), respectively. The two ribbons separate as the eruption proceeds, as shown by the stack plot of a virtual slit (Figure 1(h)) across the ribbons (with solar rotation

corrected) in Figure 2(a). Ribbon separation acts as an indicator for the ongoing magnetic reconnection processes (e.g., Priest & Forbes 2002). In Figure 2(a), vertical dashed line marks the time of first appearance of the two ribbons. Dashed red lines mark the ribbon fronts, which are visually identified, and the separation speed can be deduced from the associated slope. The separation of the ribbons is fast at first before 06:00–07:00 UT, which is consistent with the impulsive acceleration of the CME in Phase I. The separation then slows down but lasts for around five hours to around 12:00 UT, for which the signature is clearer as seen by the front of the ribbon R2, and its duration is comparable to the acceleration period of the CME in Phase II. Since magnetic reconnection plays a significant role in the CME eruption processes, the separation motion of the two ribbons indicates that for the current event reconnection processes contribute to the dynamic evolution of the CME, impulsively from the low to middle corona, and continuously for several hours in the high corona. We come back to the consequence of this reconnection in the discussion.

# 4. Contribution of Magnetic Reconnection to CME Dynamics

As presented in Section 3.1, the apparent acceleration in observations of the CME front is related to the expansion of the CME. However, as fast CMEs may experience deceleration due to the drag of the solar wind, a true CME acceleration is required to compensate for the effect of the drag and be present for the CME not to decelerate. Consequently, magnetic reconnection simultaneously contributes to both the true acceleration and the apparent acceleration (related to the expansion). The true acceleration for our event is equal to the magnitude of the deceleration caused by the drag. We then use a drag-based model (see, e.g., Cargill et al. 1996; Cargill 2004; Vršnak & Žic 2007; Subramanian et al. 2012) to estimate the magnitude of the drag effect, which is expressed as

$$a_{\text{drag}} = \frac{F_{\text{drag}}}{m_{\text{CME}}} = -\frac{C_D A_{\text{CME}} n_p m_p}{2m_{\text{CME}}}$$

$$\times (V_{\text{CME}} - V_{\text{SW}}) |V_{\text{CME}} - V_{\text{SW}}|$$
(1)

and depends on the CME and solar wind characteristics.  $C_D$  is the dimensionless drag coefficient, and here we use a hybrid viscosity model for  $C_D$  as presented by Subramanian et al. (2012).  $A_{\text{CME}}$  is the cross-sectional area of the CME, and  $A_{\rm CME} \sim \pi R_{\rm CME}^2$  where  $R_{\rm CME}$  is approximately equal to half of the lateral length of the CME.  $m_p$  and  $m_{\text{CME}}$  are the proton and CME masses, respectively. In this paper,  $m_{\text{CME}}$  is measured when the CME front is at the height of  $\sim 10 R_{\odot}$  in the C3 calibrated image by the solar software (SSW) program CME\_MASS.pro, and the value is around  $1.2 \times 10^{15}$  g. One can also refer to Vourlidas et al. (2000) for details about the mass measurement procedure.  $V_{\rm CME}$  is the CME speed, obtained by using the speed of the CME front as shown in Figure 2(d).  $n_p$  is the proton number density in the solar wind, and  $V_{\rm SW}$  is the solar wind speed. In this paper, we use a onedimensional magnetohydrodynamic numerical simulation (Hu et al. 1997) to estimate the solar wind parameters, which are dependent on the heliocentric distance. The simulations are adjusted to ensure the simulated results at a distance of 1 au are as close as possible to the in situ observations obtained from the OMNI/Wind database. Figures 4(a)–(c) show the evolution of the simulated speed, proton number density, and temperature of the solar wind, while the in situ measurements are marked by the red asterisks. We note that panel (a) further confirms that the CME is faster than the solar wind in the corona, e.g., the solar wind speed is around 200–300 km s<sup>-1</sup> in the height range  $6.5-25 R_{\odot}$ .

The estimated  $a_{drag}$  is shown in Figure 4(d), in which the filled circles are the results obtained by using the speed of the CME front from the discrete height-time measurements, and the solid curve is obtained by using the speed of the front from the quadratic fit of the height-time measurements in Phase II. The uncertainty of  $a_{drag}$  in the figure comes from the uncertainty in measuring the CME speed. Uncertainty in measurement of the CME mass is discussed later.  $|a_{drag}|$  is found to decrease from  $\sim$ 9 to  $\sim$ 4 m s<sup>-2</sup> during the propagation of the CME in the high corona. The solid curve in Figure 4(e) shows the ratio of  $|a_{\rm drag}|$  (using the values of the solid curve in (d)) to  $a_{\rm meas}$  (9.1 m s<sup>-2</sup>), with uncertainties shown by the two dashed curves. It is found that this ratio decreases from about 0.8 to 0.4, suggesting that in Phase II the contribution of magnetic reconnection to the apparent acceleration related to the expansion is comparable to or even stronger than its contribution to the true acceleration that compensates the drag for the CME.

#### 5. Discussion

We first return to our assumption that the bright core of the CME corresponds to its center. It is traditionally suggested that the bright core of the CME in coronagraphic images corresponds to prominence material. Dense prominence/ filament material is suspended in the magnetic dips at the bottom of a flux rope (Gibson et al. 2006), leading to a separation between the prominence/filament and the axis/ center of the CME. However, this scenario might be primarily true during the initiation phase of the CME; when it propagates into the mid and outer corona, the bright core can be approximately co-located with the CME center. There are three arguments supporting this assumption. First, Howard et al. (2017) and Veronig et al. (2018) presented observations showing that the inner core of the three-part coronagraph CME is not necessarily a prominence, while Veronig et al. (2018) argued that the core is still a flux rope structure. Second, the large amount of flux newly added to the core (or initial flux rope) through magnetic reconnection during the eruption (e.g., Lin & Forbes 2000; Lin et al. 2004) would keep the core in the center of the erupting structure. Third, the variation of the aspect ratio shown in Figure 3 is relatively consistent with the expectation (e.g., Savani et al. 2011) that the CME starts with a circular cross section. If the core is located at the back of the CME, the initial shape would already be very elliptical, which is contrary to past studies (e.g., Krall et al. 2001; Patsourakos et al. 2010a; Cheng et al. 2013). Note that if the core is not the center of the flux rope, this will affect the quantitative result but not the issue of acceleration itself. The CME front is still seen as accelerating to large speeds but the acceleration related to expansion would only be half of what we consider here. The acceleration of the CME front would still need to be explained.

Figure 5 shows a sketch of the CME eruption in this paper associated with a filament in the core region of the CME flux rope. This figure only shows the cross-sectional structures, and the shape of the cross section of the flux rope is designed to vary from circular to elliptical to be consistent with the

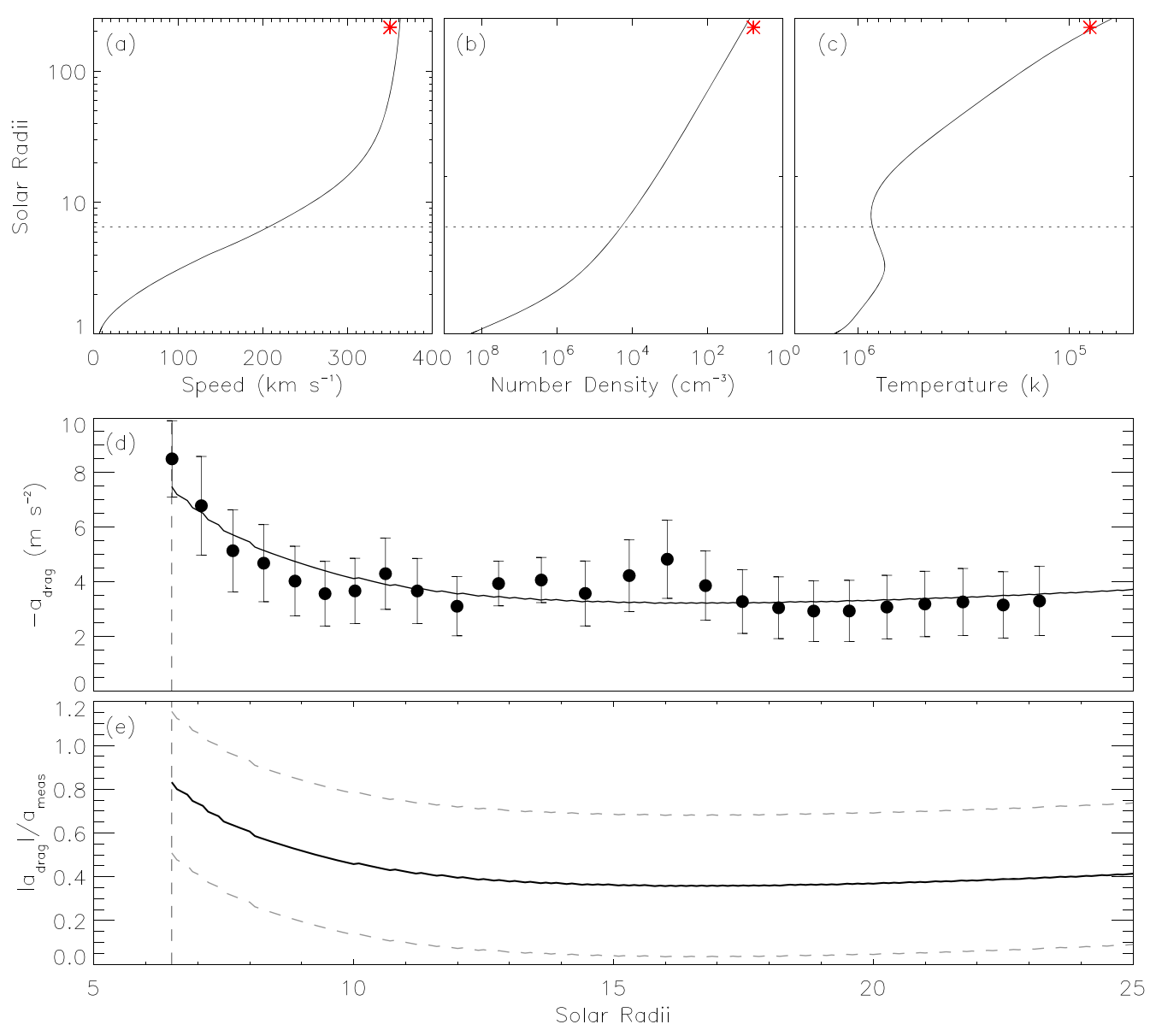


Figure 4. (a)–(c) Variation of the simulated proton speed, number density, and temperature of the solar wind with heliocentric distance, compared with the in situ observational data at 1 au (red asterisks). The horizontal dotted line indicates the distance of 6.5  $R_{\odot}$ . (d)  $a_{\rm drag}$  in the drag-based model by using the speed of the CME front based on discrete height–time measurements (filled circle) and a quadratic fit to the height–time measurements (solid curve). (e) Ratio of  $|a_{\rm drag}|$  to  $a_{\rm meas}$ . The two dashed curves indicate the lower and upper uncertainties. The vertical dashed lines in panels (d) and (e) indicate the height at 6.5  $R_{\odot}$ .

variation in aspect ratio as shown in Figure 3(b). In the left panel of the pre-eruption phase, the filament with heavy material (shaded orange) is suspended at the bottom of the initial flux rope. The flux rope then erupts in association with ongoing magnetic reconnection processes, as shown in the middle and right panels. Magnetic reconnection adds additional (poloidal) magnetic fluxes to the initial flux rope and forms the outer shells, which contributes to an additional expansion. Note that we do not show the normal expansion as the CME propagates outward, but emphasize the role of reconnection in the expansion, similar to Figure 11 in Lin et al. (2004). A posteruption arcade associated with reconnection is formed beneath the flux rope, as also seen in Figure 1(e) for the CME event. As the CME propagates upward, gravity decreases significantly, and the initial flux rope has been enveloped by a large amount of reconnected (poloidal) magnetic flux. The decreased gravity and the strong magnetic tension force from reconnected

poloidal flux may keep the initial flux rope associated with the filament (which corresponds to the bright core of the CME in coronagraph images) near the center of the CME. In addition, this scenario does not consider the mass-unloading of the filament material, which was found to facilitate the radial expansion of the CME (Jenkins et al. 2018).

We next turn our attention to the uncertainty in measurement of the CME mass. Accurate measurements are important, because (1) the calculation of  $a_{\rm drag}$  is sensitive to CME mass as clearly seen in Equation (1), and (2) the pileup of CME mass (e.g., Lugaz et al. 2005; Feng et al. 2015) may bring additional uncertainties as we set the mass as constant in the drag-based model. However, Bein et al. (2013) found that the pileup of mass is rare by analyzing the evolution of the deprojected CME mass, and Howard & Vourlidas (2018) also argued that there is no observed pileup for CMEs in the LASCO FOV by studying the variation of the electron density of the CME front. In

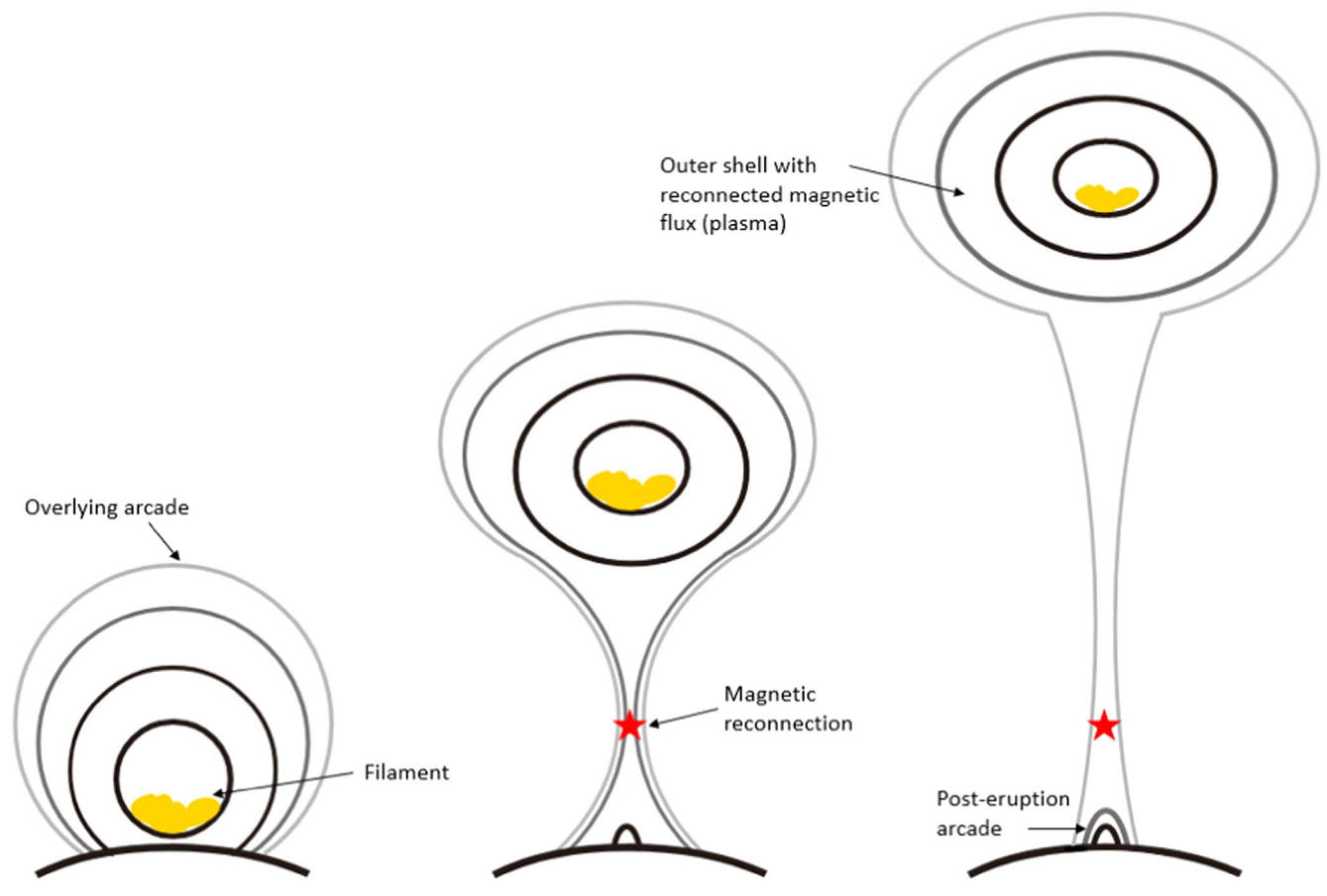


Figure 5. Sketch of a CME eruption associated with magnetic reconnection processes. Filament material is shaded orange, and the magnetic reconnection site is marked by the red asterisk. The shape of the cross section of the flux rope is designed to vary from circular to elliptical to be consistent with the variation of the aspect ratio as found in Figure 3(b).

addition, we test the influence of a  $\pm 15\%$  uncertainty of the measured mass on the comparison between CME expansion and acceleration. Still, we find similar contributions of reconnection to the expansion and acceleration.

# 6. Conclusion

The CME on 2013 February 27, originating from a quiet solar region, is found to be associated with a continuous acceleration of its front for around five hours in the high corona and even up to  $20R_{\odot}$ , though its speed has already reached  $\sim$ 700 km s<sup>-1</sup>, i.e., larger than the solar wind speed. This indicates that even fast CME events may not reach their "final" (or maximum) speed at  $20 R_{\odot}$ . The long-duration acceleration has important consequences for some heliospheric models (e.g., Odstrcil 2003; Pomoell & Poedts 2018; Scolini et al. 2019), where the inner boundary is set at  $\sim 20 R_{\odot}$ . We find that the long-duration apparent acceleration of the CME front is caused by the CME's own expansion, which further suggests the importance of considering expansion in studying CME dynamics and in those heliospheric models that usually assume a uniform speed distribution within the CME. For a discussion of including expansion in the initiation of a CME at  $20 R_{\odot}$  in a heliospheric model, see Scolini et al. (2019). A long-duration magnetic reconnection occurs after the eruption, which contributes to the evolution of the CME dynamics. For this CME, especially when it is in the high corona, magnetic reconnection results in (1) an apparent acceleration related to

the expansion and (2) a true acceleration compensating the deceleration caused by the drag of the solar wind. A quantitative comparison between the expansion and true acceleration of the CME in the high corona indicates that the contribution of reconnection to the expansion of the CME is comparable to the contribution to its true acceleration in that height range. In addition, a study about the Alfvén point being located at up to  $12-15\,R_\odot$  (DeForest et al. 2014), and a recent paper showing that the Alfvén point (or surface) even reaches as high as  $\sim 19\,R_\odot$  using the observations from the Parker Solar Probe (Kasper et al. 2021), support the possibility of magnetic reconnection continuously contributing to the CME dynamics from the low to high corona.

We acknowledge the use of the data from SOHO, STEREO, and OMNI/Wind. SOHO is a mission of international cooperation between ESA and NASA. Research for this work was made possible by NASA grants 80NSSC19K0831, 80NSSC20K0700, and 80NSSC20K0431. N.A.-H. thanks the grants from NSF AGS-1954983 and NASA ECIP 80NSSC21K0463.

### **ORCID iDs**

Bin Zhuang https://orcid.org/0000-0002-5996-0693

Noé Lugaz https://orcid.org/0000-0002-1890-6156

Manuela Temmer https://orcid.org/0000-0003-4867-7558

Tingyu Gou https://orcid.org/0000-0003-0510-3175

Nada Al-Haddad https://orcid.org/0000-0002-0973-2027

#### References

```
Balmaceda, L. A., Vourlidas, A., Stenborg, G., & Cyr, O. C., St. 2020, SoPh,
   295, 107
Bein, B. M., Berkebile-Stoiser, S., Veronig, A. M., et al. 2011, ApJ, 738, 191
Bein, B. M., Temmer, M., Vourlidas, A., Veronig, A. M., & Utz, D. 2013, ApJ,
   768, 31
Brueckner, G. E., Howard, R. A., Koomen, M. J., et al. 1995, SoPh, 162, 357
Cargill, P. J. 2004, SoPh, 221, 135
Cargill, P. J., Chen, J., Spicer, D. S., & Zalesak, S. T. 1996, JGR, 101, 4855
Cheng, X., Zhang, J., Ding, M. D., Liu, Y., & Poomvises, W. 2013, ApJ,
  763, 43
DeForest, C. E., Howard, T. A., & McComas, D. J. 2014, ApJ, 787, 124
Domingo, V., Fleck, B., & Poland, A. I. 1995, SoPh, 162, 1
Farrugia, C. J., Burlaga, L. F., Osherovich, V. A., et al. 1993, JGR, 98, 7621
Feng, L., Wang, Y., Shen, F., et al. 2015, ApJ, 812, 70
Forbes, T. G. 2000, JGR, 105, 23153
Gibson, S. E., Foster, D., Burkepile, J., de Toma, G., & Stanger, A. 2006, ApJ,
  641, 590
Gopalswamy, N., Lara, A., Lepping, R. P., et al. 2000, GeoRL, 27, 145
Gou, T., Veronig, A. M., Liu, R., et al. 2020, ApJL, 897, L36
Howard, R. A., Moses, J. D., Vourlidas, A., et al. 2008, SSRv, 136, 67
Howard, R. A., & Vourlidas, A. 2018, SoPh, 293, 55
Howard, T. A., DeForest, C. E., Schneck, U. G., & Alden, C. R. 2017, ApJ,
  834, 86
Hu, Y. Q., Esser, R., & Habbal, S. R. 1997, JGR, 102, 14661
Illing, R. M. E., & Hundhausen, A. J. 1986, JGR, 91, 10951
Jenkins, J. M., Long, D. M., van Driel-Gesztelyi, L., & Carlyle, J. 2018, SoPh,
Kaiser, M. L., Kucera, T. A., Davila, J. M., et al. 2008, SSRv, 136, 5
Kasper, J. C., Klein, K. G., Lichko, E., et al. 2021, PhRvL, 127, 255101
Kilpua, E., Lugaz, N., Mays, M. L., & Temmer, M. 2019, SpWea, 17, 498
Krall, J., Chen, J., Duffin, R. T., Howard, R. A., & Thompson, B. J. 2001, ApJ,
Lamy, P. L., Floyd, O., Boclet, B., et al. 2019, SSRv, 215, 39
Lin, J., & Forbes, T. G. 2000, JGR, 105, 2375
```

Lin, J., Raymond, J. C., & van Ballegooijen, A. A. 2004, ApJ, 602, 422

Lugaz, N., Manchester, W. B. I., & Gombosi, T. I. 2005, ApJ, 627, 1019

Lugaz, N., Farrugia, C. J., Winslow, R. M., et al. 2017, ApJ, 848, 75

```
Michalek, G., Gopalswamy, N., & Yashiro, S. 2009, SoPh, 260, 401
Michalek, G., Gopalswamy, N., Yashiro, S., & Bronarska, K. 2015, SoPh,
  290, 903
Odstrcil, D. 2003, AdSpR, 32, 497
Patsourakos, S., Vourlidas, A., & Kliem, B. 2010a, A&A, 522, A100
Patsourakos, S., Vourlidas, A., & Stenborg, G. 2010b, ApJL, 724, L188
Pomoell, J., & Poedts, S. 2018, JSWSC, 8, A35
Priest, E. R., & Forbes, T. G. 2002, A&ARv, 10, 313
Sachdeva, N., Subramanian, P., Colaninno, R., & Vourlidas, A. 2015, ApJ,
  809, 158
Savani, N. P., Owens, M. J., Rouillard, A. P., et al. 2011, ApJ, 731, 109
Schwenn, R., dal Lago, A., Huttunen, E., & Gonzalez, W. D. 2005, AnGeo,
Scolini, C., Rodriguez, L., Mierla, M., Pomoell, J., & Poedts, S. 2019, A&A,
  626, A122
Song, H. Q., Chen, Y., Ye, D. D., et al. 2013, ApJ, 773, 129
Subramanian, P., Lara, A., & Borgazzi, A. 2012, GeoRL, 39, L19107
Temmer, M., Veronig, A. M., Kontar, E. P., Krucker, S., & Vršnak, B. 2010,
   ApJ, 712, 1410
Temmer, M., Veronig, A. M., Vršnak, B., et al. 2008, ApJL, 673, L95
Thernisien, A., Vourlidas, A., & Howard, R. A. 2009, SoPh, 256, 111
Thernisien, A. F. R., Howard, R. A., & Vourlidas, A. 2006, ApJ, 652, 763
Veronig, A. M., Podladchikova, T., Dissauer, K., et al. 2018, ApJ, 868, 107
Vourlidas, A., Subramanian, P., Dere, K. P., & Howard, R. A. 2000, ApJ,
  534, 456
Vourlidas, A., Wu, S. T., Wang, A. H., Subramanian, P., & Howard, R. A.
  2003, ApJ, 598, 1392
Vršnak, B. 2001, SoPh, 202, 173
Vršnak, B. 2008, AnGeo, 26, 3089
Vršnak, B., Maričić, D., Stanger, A. L., et al. 2007, SoPh, 241, 85
Vršnak, B., Maričić, D., Stanger, A. L., & Veronig, A. 2004a, SoPh, 225, 355
Vršnak, B., Ruždjak, D., Sudar, D., & Gopalswamy, N. 2004b, A&A, 423, 717
Vršnak, B., & Žic, T. 2007, A&A, 472, 937
Zhang, J., Dere, K. P., Howard, R. A., Kundu, M. R., & White, S. M. 2001,
  ApJ, 559, 452
Zhang, J., Dere, K. P., Howard, R. A., & Vourlidas, A. 2004, ApJ, 604, 420
Zhu, C., Qiu, J., Liewer, P., et al. 2020, ApJ, 893, 141
Zhuang, B., Lugaz, N., Gou, T., Ding, L., & Wang, Y. 2020, ApJ, 901, 45
Zhuang, B., Wang, Y., Shen, C., & Liu, R. 2018, E&PP, 2, 112
```